

Evidence for Two Dimensional Anisotropic Luttinger Liquids at Millikelvin Temperatures

Guo Yu^{1,2,#}, Pengjie Wang^{1,#}, Ayelet J. Uzan¹, Yanyu Jia¹, Michael Onyszcak¹, Ratnadwip Singha³, Xin Gui³, Tiancheng Song¹, Yue Tang¹, Kenji Watanabe⁴, Takashi Taniguchi⁵, Robert J. Cava³, Leslie M. Schoop³, Sanfeng Wu^{1,*}

¹Department of Physics, Princeton University, Princeton, New Jersey 08544, USA

²Department of Electrical and Computer Engineering, Princeton University, Princeton, New Jersey 08544, USA

³Department of Chemistry, Princeton University, Princeton, New Jersey 08544, USA

⁴Research Center for Functional Materials, National Institute for Materials Science, 1-1 Namiki, Tsukuba 305-0044, Japan

⁵International Center for Materials Nanoarchitectonics, National Institute for Materials Science, 1-1 Namiki, Tsukuba 305-0044, Japan

These authors contributed equally to this work

* Email: sanfengw@princeton.edu

Abstract

While Landau's Fermi liquid theory provides the standard description for two- and three-dimensional (2D/3D) conductors, the physics of interacting one-dimensional (1D) conductors is governed by the distinct Luttinger liquid (LL) theory. Can a LL-like state, in which electronic excitations are fractionalized modes, emerge in a 2D system as a stable zero-temperature phase? This long-standing question, first brought up by Anderson decades ago, is crucial in the study of non-Fermi liquids but remains unsettled. A recent experiment identified a moiré superlattice of twisted bilayer tungsten ditelluride (tWTe₂) with a small interlayer twist angle as a 2D host of the LL physics at temperatures of a few kelvins. Here we report experimental evidence for a 2D anisotropic LL state in a substantially reduced temperature regime, down to at least 50 mK, spontaneously formed in a tWTe₂ system with a twist angle of $\sim 3^\circ$. While the system is metallic-like and nearly isotropic above 2 K, a dramatically enhanced electronic anisotropy develops in the millikelvin regime, featuring distinct transport behaviors along two orthogonal in-plane directions. In the strongly anisotropic phase, we observe transport characteristics of a 2D LL phase, i.e., the universal power law scaling behaviors in across-wire conductance and a zero-bias dip in the differential resistance along the wire direction. Our results represent a step forward in the search for stable LL physics beyond 1D and related unconventional quantum matter.

Main

The Luttinger liquid (LL) theory of 1D interacting conductors offers a demonstration of a gapless electronic phase beyond the standard Fermi liquid (FL) paradigm^{1,2}. Distinct features of a LL owing to strong correlations include the power-law suppression of the density of state (DOS) at the Fermi energy and the fractionalization of electronic excitations into collective modes associated separately with spin and charge degrees of freedom. These appealing properties of a 1D LL have led Anderson to explore the possibility of LL-like physics in dimensions higher than one for explaining the unusual phenomena of cuprate superconductors³⁻⁶. However, the application of this novel concept in cuprates

has been difficult, despite many attempts³⁻⁶. In general, the search for non-Fermi liquid physics in higher-than-one dimensional systems is an important but challenging topic.

Alternatively, theoretical searches for 2D or 3D non-Fermi liquids were also put forward in the context of coupled-wire constructions⁷⁻¹¹, where identical parallel 1D nanowires, each being described by the LL theory, are placed together to form 2D arrays or 3D networks. One key question is whether the LL physics survives in the coupled-wire systems at vanishing temperatures when interwire hopping is turned on. Similar problems have been considered in the study of quasi-1D organic conductors¹², which may be regarded as weakly coupled wires. Typically, a crossover temperature T^* from the LL state at intermediate temperatures to a 2D FL or gapped state at low temperatures exists and may be estimated^{1,7,13} as $T^* \sim t_{\perp}(t_{\perp}/t_{\parallel})^{\eta/(1-\eta)}$, where t_{\perp} (t_{\parallel}) is the interwire (intrawire) hopping term and η is the power law exponent of the DOS at the 1D Fermi surface¹³. Here η reflects the intrawire interaction strength (see illustration in Fig. 1a & b) and $t_{\perp} < t_{\parallel}$ in a coupled wire setting. Experimentally, T^* in organic quasi-1D conductors is typically tens of kelvins¹², below which the LL description is invalid. Interestingly, in the above expression, one readily sees that the intrawire interaction suppresses T^* . If η is large enough, i.e., $\eta > 1$, T^* in principle vanishes, indicating a new regime where single-particle hopping is irrelevant^{1,7,13} even down to zero temperature. In realistic systems, other competing phases, especially those arising from two-particle hopping processes, become important in this regime and provide instabilities to the LL state. Evaluating competing phases, such as charge density wave, FL and superconducting states, is indeed the key focus of multiple theoretical works⁷⁻¹¹ in the early 2000s, which carefully investigated the phase diagram of a 2D array of coupled LL. Under some fine-tuned interactions, they predicted, remarkably, the possible existence of a stable anisotropic phase in which both single- and two-particle interwire hopping processes are all irrelevant, i.e., a phase akin to the LL surviving as a zero-temperature ground state in a small parameter space. This anisotropic 2D phase, coined a “sliding LL”⁹⁻¹¹ or “smectic metal”⁸, is surrounded by its competing orders and its realization requires careful control of parameters in the coupled wires.

An experimental realization of coupled-wire constructions in a controllable setting is however challenging. Very recently, new material systems have been identified for investigating LL physics beyond 1D, notably including the moiré superlattice of twisted bilayer WTe_2 ($t\text{WTe}_2$)¹⁴ and a quasi-2D material $\eta\text{-Mo}_4\text{O}_{11}$ ¹⁵. Evidence for LL physics has been shown down to 1.8 K in $t\text{WTe}_2$ with a twist angle near 5° and ~ 10 K in $\eta\text{-Mo}_4\text{O}_{11}$ (see the table in Fig. 1c). An essential question is whether the LL state can survive in any realistic systems down to the lowest achievable temperature in experiments, particularly in the millikelvin regime. In this work, we address this fundamental question for establishing the concept of a 2D LL, based on $t\text{WTe}_2$ moiré superlattices. The exceptional tunability of electronic properties by moiré engineering places $t\text{WTe}_2$ as an outstanding system for such studies.

$t\text{WTe}_2$ Moiré Lattice and Device Design

Owing to the rectangular unit cell of monolayer WTe_2 (Fig. 1d), the super unit cell of the moiré lattice in $t\text{WTe}_2$, when the twisted angle θ is small, is also a rectangle but large. Fig. 1e & f illustrate the atomic structure of $t\text{WTe}_2$, where only the W atoms are shown to better visualize it. The moiré pattern clearly resembles the coupled-wire lattice shown in Fig. 1a. By tuning the twist angle, one can arbitrarily choose the size of the supercell in a wide range, which alters key parameters that determine its ground phases. Our previous work revealed that $t\text{WTe}_2$ at $\theta \sim 5^\circ$ indeed develops LL physics below ~ 30 K

on the hole-rich side¹⁴, evidenced by the emergence of large transport anisotropy and power law scaling behaviors of its conductance. There the LL transport characteristics were confirmed down to 1.8 K, below which the across-wire resistance becomes too large ($> 10 \text{ M}\Omega$) to be resolved quantitatively¹⁴, preventing transport access to the physics in the sub-kelvin regime. The essential question of whether the LL description is valid at millikelvin temperatures in tWTe₂, or any 2D/3D experimental system, remains unknown.

In this work we focus on tWTe₂ with a smaller θ , near 3° , where the moiré cell is larger (interwire distance $d \sim 12 \text{ nm}$, as shown in Fig. 1e) and the energy scale is in principle smaller. Similar to previous reports^{14,16,17}, we fabricate devices with tWTe₂ fully encapsulated by top and bottom hexagonal boron nitride (hBN) dielectrics and metal (Pd) gate (see Fig. 1g for device structure). A thin layer of selectively etched hBN is inserted between the tWTe₂ and metal (Au or Pd) electrodes, to ensure direct electric contacts to the tWTe₂ interior (indicated by the red squares in the optical image of a typical device shown in Fig. 1h). With this device geometry, contributions to transport from the nearby monolayer WTe₂ regions, as well as its edge modes, are minimized. Details of device fabrication are illustrated in Methods and Extended Data Fig. 1. The application of gate voltages varies the carrier density in the sample. We quantify the gate-induced doping as $n_g \equiv \epsilon_r \epsilon_0 (V_{\text{tg}}/d_{\text{tg}} + V_{\text{bg}}/d_{\text{bg}})/e$, where V_{tg} (V_{bg}) is the top (bottom) gate voltage; d_{tg} (d_{bg}) is the thickness of the top (bottom) hBN dielectric; ϵ_0 , ϵ_r and e are respectively the vacuum permittivity, relative dielectric constant of hBN, and elementary charge. The choice of near 3° twist angle is based on systematic studies of tWTe₂ with a range of small twist angles (see Extended Data Figs. 2-4). The much smaller resistivity, compared to $\sim 5^\circ$ devices or the monolayer, together with a large emergent anisotropy near this angle, provides a key condition for us to evaluate the LL transport characteristics quantitatively down to temperatures as low as $\sim 50 \text{ mK}$.

Emergent Anisotropy at Millikelvin Temperatures

Fig. 2a plots resistance measured in device 1 ($\theta \sim 3^\circ$) under varying gate voltages at a sample temperature, T , of 4 K. The maximum is only $\sim 20 \text{ k}\Omega$ and no substantial transport anisotropy is found; both aspects are distinct from the tWTe₂ with $\theta \sim 5^\circ$ at the same temperature¹⁴, highlighting the key role of θ . Interestingly, an exceptionally large transport anisotropy develops at millikelvin temperatures, where the easy and hard transport directions can be clearly identified by measuring resistances between neighboring probes in the ring contact geometry (see Extended Data Fig. 5). To quantify the anisotropy, we carefully examine four-probe resistances (R_{easy} and R_{hard}) measured in both directions (as illustrated in Fig. 2b). Fig. 2c & d plots R_{hard} and R_{easy} , respectively, as a function of V_{bg} at a fixed $V_{\text{tg}} = 2.00 \text{ V}$, taken at various T below 2 K. One clearly sees a dramatic increase of R_{hard} on the hole-rich side and near the charge neutrality point (CNP) when T is lowered. At 50 mK, R_{hard} reaches a value of more than $1 \text{ M}\Omega$. In sharp contrast, this strong increase is absent on the electron-rich side and, markedly, for R_{easy} at all doping. We define an anisotropy ratio $\beta \equiv R_{\text{hard}}/R_{\text{easy}}$ (Fig. 2e). Near CNP and with hole doping, β is large, reaching 10,000 at 50 mK. Warming the sample β decreases dramatically (Fig. 2f). Anisotropy is absent in the electron-rich regime at any T .

The distinct transport along the two orthogonal directions (easy *v.s.* hard) manifests itself not only in the strong anisotropy (large β), but also in its bias-dependence. Fig. 2g-i examine the effects of a d.c. bias (V) applied to the source contact in device 1, at $V_{\text{tg}} = 1.00 \text{ V}$ and $V_{\text{bg}} = -3.00 \text{ V}$ (indicated by the white cross in Fig. 2a), where a large β is seen. Near zero bias, a large peak is clearly seen when transport is along the hard direction (Fig. 2g), exhibiting an insulating-like behavior. Warming up the device to $\sim 2 \text{ K}$, the curve flattens. In sharp contrast, the same measurement along the easy direction yields a

clear zero bias dip (Fig. 2h). Similar behavior is found in device 2 ($\theta \sim 3.5^\circ$), as shown in Extended Data Fig. 6. A consistent zero bias dip is also seen in a $\sim 5^\circ$ tWTe₂ device (Extended Data Fig. 7). At first glance, this dip feature resembles that of a superconductor. However, it cannot be suppressed by magnetic fields (Extended Data Fig. 6) and only appears when it is measured along the easy direction. Instead of arising from superconductivity, this remarkable feature can be well explained by the spontaneous formation of a new phase consisting of a 2D array of 1D electronic channels, as illustrated by the grey lines in Fig. 2b. At small bias, this new phase develops and the current flowing between source and drain contacts are restricted to the 1D channels connecting them. Consequently, current flow is minimized between the voltage probes placed nearby, yielding a vanishing voltage, i.e., the zero-bias dip. At high V or high T , this strongly anisotropic phase is destroyed (Fig. 2i), leading to a finite voltage between the two probes. The shoulder next to the zero-bias dip (Fig. 2h) signifies the transition between the anisotropic phase to an isotropic one at high V .

LL Characteristics down to 50 mK

We next examine transport characteristics expected for a LL state, namely the power law scaling behavior of the conductance. Conventionally, in a single 1D wire system one may measure tunneling conductance from a Fermi liquid lead to the wire^{18–22}. In our case of an array of parallel 1D wires in the moiré system, electron transport in the hard direction involves tunneling between wires, providing an excellent opportunity for examining power law behaviors without the need of an external tunneling probe¹⁴. One consequence of the LL physics is that the across-wire conductance $G(T) \equiv 1/R_{\text{hard}} \propto T^\alpha$ where the exponent α reflects the power law suppression of the DOS near the Fermi energy^{7–11,13,23}. This is indeed seen in the strongly anisotropic regime of our devices, as shown in Fig. 3a for device 1. At this gate configuration, we find that a value of $\alpha \sim 1.53$ captures well the low- T conductance from ~ 500 mK down to 50 mK. A transition to the high- T isotropic phase occurs near ~ 1 K, above which only a weak T -dependence is seen in G . In Extended Data Fig. 8, we further confirm that neither an exponential form expected for an activation gap nor the variable-range hopping form for localization²⁴ can describe the observed conductance at millikelvin temperatures.

Another essential LL feature lies in the bias-dependent differential conductance, i.e., $dI/dV \propto V^\alpha$ when $eV \gg k_B T$, where k_B is the Boltzmann constant. The same exponent α must be seen here as in the above $G(T)$ since it reflects the same suppression of DOS. In other words, LL physics¹ dictates that the scaled conductance $(dI/dV)/T^\alpha$ is only a function of $eV/k_B T$. Fig. 3b plots the measured dI/dV as a function of V varied from 10 μ V to ~ 1 mV, taken at various T . Remarkably, all data points, taken in the parameter space spanned over two decades in V and one decade in T , collapse into a single curve in the scaled plot (Fig. 3c)! The only parameter used here is α , the same one extracted from $G(T)$ (Fig. 3a). Hence the exponent α provides a key description of the transport behaviors of the system, well consistent with the emergence of LL physics in the moiré system. In a simplified argument where only an effective intrawire Fermi surface exponent η is considered, a calculation for across wire transport yields $\alpha = 2\eta - 1$ ¹³. If this is valid, we estimate $\eta \sim 1.26$, a value that is larger than one. It is therefore consistent with the condition for the single-particle interwire hopping to be irrelevant, as discussed in Fig. 1b. We note that in realistic system, two-particle hopping process are also important in this regime and hence the interactions shall be described by more complex parameters that involve both interwire and intrawire interactions^{7–11}, instead of a single η . In that case, dimensional crossover and competing orders provide new instabilities to the LL phase. Theoretically,

competing phases indeed reside in most regions in the calculated phase diagram, expect that the predicted sliding LL under fine-tuned interactions offers a possible realization of a 2D LL phase at vanishing temperatures⁷⁻¹¹. The experimental consequence is that although the wires are closely packed, the system, driven by interactions, behaves as an array of “independent” LL wires, and that transport across the wires is fully suppressed unless a finite temperature or bias is applied. From this perspective, the vanishing dV/dI (Fig. 2h) in the zero-bias dip measured along the wires, which does indicate that the wires are effectively independent, provides an additional key characterization of the observed phase in $tWTe_2$. We believe our observations of the dramatic zero-bias dip along the wire, together with the large anisotropy and the power law across-wire conductance, indicates the emergence of a highly intriguing new phase akin to the proposed “sliding LL”, although the understanding of the exact mechanism requires substantial future developments in both theory and experiments.

The observations are reproduced in different contact geometries (Extended Data Fig. 9) and in device 2, as shown in Fig. 3d-f and Extended Data Fig. 6. We again highlight that here the LL description is valid down to 50 mK, an unprecedented regime. This temperature is well below the energy scale (\sim meV) of the hopping and interaction terms in the system. Any dimensional crossover, if exists, must be lower than this temperature.

Electronic Phase Diagram

We discuss the gate-tuned phase diagram of $tWTe_2$ at this small twist angle based on device 2. Fig. 4a presents the gate-dependent anisotropy map taken at 150 mK, where the red color indicates large β . $G(T)$ and dI/dV were recorded at selected typical locations, as indicated in the map. Power law behaviors are found together with strong anisotropy for locations labeled as c-f, while regions of g, h and i show clear deviations from a power law (Fig. 4b). Particularly, at c-f, electronic transport exhibits universal scaling characteristics (Fig. 4c-f) qualitatively like the observations in Fig. 3, hence implying the formation of a 2D anisotropic LL phase robust down to 50 mK. This region occurs near CNP, with n_g roughly within $\pm 4 \times 10^{12} \text{ cm}^{-2}$. We find that while LL behaviors are sensitive to carrier density, the displacement field (D) effect is less dramatic especially if D is not too large. At high D , we do find a drop in the power law exponent (Extended Data Fig. 10), potentially indicating a transition to a different phase if D is further increased. On the electron dominant side (e.g., location g), one sees almost no T - or V - dependence of the conductance, indicating a transition to a metallic-like state with an Ohmic behavior (Fig. 4g). On the hole dominant side, although strong transport anisotropy starts to develop below ~ 1 K, the conductance deviates from the power law typically when T is further lowered to, e.g., ~ 400 mK for location i and ~ 100 mK for h, as shown in Fig. 4b, h & i. The data suggests a crossover to a non-LL phase at lower T . In Fig. 4j we summarize the observation by presenting a preliminary phase diagram describing $tWTe_2$ at this twist angle, under varying T and n_g (here we limit the electric displacement field to small values for simplicity). The presence of a finite parameter region (blue) that hosts an anisotropic 2D phase mimicking the LL is the key finding.

Discussion and Summary

In this work, we experimentally address the long-standing question of whether a 2D non-Fermi liquid phase resembling a LL can exist as a stable ground state. We conclude that such a phase does develop in the $tWTe_2$ moiré system down to at least 50 mK. We note that at this early stage a concrete theoretical modeling of this strongly correlated phase is still lacking. It is a challenging task to compute

the electronic structure of $tWTe_2$ moiré system even at the single particle level due to the large number of atoms and orbits involved in each moiré cell, together with the presence of spin-orbital coupling and possible superlattice reconstructions. Future theoretical consideration would also need to consider strong electron interactions, which seems to be essential in the system. The phenomenology of a 2D sliding LL, independently proposed two decades ago based on theoretical analysis of coupled-wire models⁷⁻¹¹, is well consistent with our observations here, including the large transport anisotropy, power law conductance across the wires and the vanishing differential resistance along the wires. However, establishing exact connections between the experiments and the models requires future efforts from both theory and experimental sides. Our experiments open new possibilities to further study topics related to 2D LL ground states and phase transitions, including spin-charge separation^{1,20,25}, novel quantum oscillations and quantum Hall effects in non-Fermi liquids.²⁶⁻²⁸

References

1. Giamarchi, T. *Quantum Physics in One Dimension*. (Oxford University Press, 2003). doi:10.1093/acprof:oso/9780198525004.001.0001.
2. Haldane, F. D. M. ‘Luttinger liquid theory’ of one-dimensional quantum fluids. I. Properties of the Luttinger model and their extension to the general 1D interacting spinless Fermi gas. *J. Phys. C: Solid State Phys.* **14**, 2585 (1981).
3. Anderson, P. W. ‘Luttinger-liquid’ behavior of the normal metallic state of the 2D Hubbard model. *Phys. Rev. Lett.* **64**, 1839–1841 (1990).
4. Anderson, P. W. ‘Confinement’ in the one-dimensional Hubbard model: Irrelevance of single-particle hopping. *Phys. Rev. Lett.* **67**, 3844–3847 (1991).
5. Strong, S. P., Clarke, D. G. & Anderson, P. W. Magnetic Field Induced Confinement in Strongly Correlated Anisotropic Materials. *Phys. Rev. Lett.* **73**, 1007–1010 (1994).
6. Anderson, P. W. Hall effect in the two-dimensional Luttinger liquid. *Phys. Rev. Lett.* **67**, 2092–2094 (1991).
7. Wen, X. G. Metallic non-Fermi-liquid fixed point in two and higher dimensions. *Phys. Rev. B* **42**, 6623–6630 (1990).
8. Emery, V. J., Fradkin, E., Kivelson, S. A. & Lubensky, T. C. Quantum Theory of the Smectic Metal State in Stripe Phases. *Phys. Rev. Lett.* **85**, 2160–2163 (2000).
9. Sondhi, S. L. & Yang, K. Sliding phases via magnetic fields. *Phys. Rev. B* **63**, 054430 (2001).
10. Vishwanath, A. & Carpentier, D. Two-Dimensional Anisotropic Non-Fermi-Liquid Phase of Coupled Luttinger Liquids. *Phys. Rev. Lett.* **86**, 676–679 (2001).
11. Mukhopadhyay, R., Kane, C. L. & Lubensky, T. C. Sliding Luttinger liquid phases. *Phys. Rev. B* **64**, 045120 (2001).
12. Biermann, S., Georges, A., Giamarchi, T. & Lichtenstein, A. Quasi One-Dimensional Organic Conductors: Dimensional Crossover and Some Puzzles. in *Strongly Correlated Fermions and Bosons in Low-Dimensional Disordered Systems* (eds. Lerner, I. V., Althuler, B. L., Fal’ko, V. I. & Giamarchi, T.) 81–102 (Springer Netherlands, 2002). doi:10.1007/978-94-010-0530-2_5.
13. Georges, A., Giamarchi, T. & Sandler, N. Interchain conductivity of coupled Luttinger liquids and organic conductors. *Phys. Rev. B* **61**, 16393–16396 (2000).
14. Wang, P. *et al.* One-dimensional Luttinger liquids in a two-dimensional moiré lattice. *Nature* **605**, 57–62 (2022).
15. Du, X. *et al.* Crossed Luttinger liquid hidden in a quasi-two-dimensional material. *Nat. Phys.* **19**, 40–45 (2023).
16. Wang, P. *et al.* Landau quantization and highly mobile fermions in an insulator. *Nature* **589**, 225–229 (2021).
17. Jia, Y. *et al.* Evidence for a monolayer excitonic insulator. *Nat. Phys.* **18**, 87–93 (2022).
18. Bockrath, M. *et al.* Luttinger-liquid behaviour in carbon nanotubes. *Nature* **397**, 598–601 (1999).
19. Yao, Z., Postma, H. W. C., Balents, L. & Dekker, C. Carbon nanotube intramolecular junctions. *Nature* **402**, 273–276 (1999).
20. Deshpande, V. V., Bockrath, M., Glazman, L. I. & Yacoby, A. Electron liquids and solids in one dimension. *Nature* **464**, 209–216 (2010).
21. Chang, A. M. Chiral Luttinger liquids at the fractional quantum Hall edge. *Rev. Mod. Phys.* **75**, 1449–1505 (2003).
22. Dudy, L., Aulbach, J., Wagner, T., Schäfer, J. & Claessen, R. One-dimensional quantum matter: gold-induced nanowires on semiconductor surfaces. *J. Phys.: Condens. Matter* **29**, 433001 (2017).
23. Clarke, D. G., Strong, S. P. & Anderson, P. W. Incoherence of single particle hopping between Luttinger liquids. *Phys. Rev. Lett.* **72**, 3218–3221 (1994).

24. Efros, A. L. & Shklovskii, B. I. Coulomb gap and low temperature conductivity of disordered systems. *J. Phys. C: Solid State Phys.* **8**, L49 (1975).
25. Auslaender, O. M. *et al.* Spin-Charge Separation and Localization in One Dimension. *Science* **308**, 88–92 (2005).
26. Kane, C. L., Mukhopadhyay, R. & Lubensky, T. C. Fractional Quantum Hall Effect in an Array of Quantum Wires. *Phys. Rev. Lett.* **88**, 036401 (2002).
27. Teo, J. C. Y. & Kane, C. L. From Luttinger liquid to non-Abelian quantum Hall states. *Phys. Rev. B* **89**, 085101 (2014).
28. Tam, P. M. & Kane, C. L. Nondiagonal anisotropic quantum Hall states. *Phys. Rev. B* **103**, 035142 (2021).
29. Ali, M. N. *et al.* Correlation of crystal quality and extreme magnetoresistance of WTe₂. *EPL* **110**, 67002 (2015).
30. Kim, K. *et al.* van der Waals Heterostructures with High Accuracy Rotational Alignment. *Nano Lett.* **16**, 1989–1995 (2016).
31. Cao, Y. *et al.* Superlattice-Induced Insulating States and Valley-Protected Orbits in Twisted Bilayer Graphene. *Phys. Rev. Lett.* **117**, 116804 (2016).

Method

Sample Fabrication

We follow a similar process of crystal growth and device fabrication used in our previous works on WTe_2 ^{14,16,17,29}. We used Pd metal bottom and top gates in both devices. To create the metal bottom gate, a ~ 2 nm Ti/ ~ 6 nm Pd film was deposited onto an insulating Si/SiO₂ substrate using the standard e-beam lithography (EBL) and metal deposition tools. The bottom hBN was then transferred onto the metal bottom gate in a dry-transfer setup, followed by EBL and metal deposition of the metal contacts (~ 2 nm Ti/ ~ 6 nm Pd for device 1 and ~ 2 nm Ti/ ~ 6 nm Au for device 2). After a tip-cleaning process using an atomic force microscope (AFM), a thin hBN was transferred to cover the metal electrodes and selective areas of the thin hBN were etched using EBL and reactive ion etching (RIE) techniques. The top metal gate consists of either a ~ 15 nm Pd layer (device 1) or a ~ 3 nm Ti/ ~ 12 nm Pd layer (device 2), which was deposited onto exfoliated hBN flakes with the help of EBL for defining the location and shape. Monolayer WTe_2 was exfoliated on Si/SiO₂ substrates in an Ar-filled glovebox. The top metal/hBN stack was picked up as a whole followed by the ‘tear-and-stack’^{30,31} procedures that create the $t\text{WTe}_2$ stack. All processes that involve WTe_2 were conducted in the glovebox. A cartoon illustration of the fabrication process can be found in Extended Data Fig. 1.

Transport Measurement at Ultralow Temperatures

Electronic transport measurements were performed in a Bluefors dilution refrigerator with bottom loading probe system. The probe base temperature is ~ 24 mK. Thermocoax wires and a series of heat sinks are used to keep the electron temperature low. We calibrated the electron temperatures using a high-quality GaAs quantum well sample based on the activation behavior of a fractional quantum Hall state and found that the electron temperature in our setup starts to deviate from the probe thermometer temperature only below 45 mK. We therefore perform measurements in this work at temperatures of 50 mK or above.

In the measurements, an a.c. excitation of typically 10 μV with a frequency of 7 \sim 17 Hz, together with a d.c. bias, was applied to the source electrode via a Keysight 33511B function generator. Current and voltage signals were collected using lock-in amplifiers after a current (DL Instruments model 1211, with an internal impedance of 20 Ω) and voltage pre-amplifier (DL Instruments model 1201, with an internal impedance of 100 M Ω) to improve the signal. Gate voltages were applied via Keithley 2400 or 2450. The setup can reliably measure four-probe resistance up to a few M Ω and all data presented in this work are in the reliable regime.

Acknowledgements

We acknowledge discussions with Y. H. Kwan, S. A. Parameswaran, and S. L. Sondhi. This work was supported by ONR through a Young Investigator Award (N00014-21-1-2804) to S.W. Measurement systems and data collection were supported by NSF through a CAREER award (DMR-1942942) to S.W. Materials synthesis and device fabrication were partially supported by the Materials Research Science and Engineering Center (MRSEC) program of the NSF (DMR-2011750) through support to R.J.C., L.M.S., and S.W. S.W. and L.M.S. acknowledge support from the Eric and Wendy Schmidt Transformative Technology Fund at Princeton. A.J.U. acknowledges support from the Rothschild Foundation and the Zuckerman Foundation. K.W. and T.T. acknowledge support from the JSPS

KAKENHI (Grant Numbers 19H05790, 20H00354, and 21H05233). L.M.S. acknowledges support from the Gordon and Betty Moore Foundation through Grants GBMF9064, the David and Lucile Packard Foundation and the Sloan Foundation.

Author contributions

G.Y. and P.W. fabricated the devices, performed measurements, and analyzed the data, assisted by A. J.U., Y.J., M.O., T.S., and Y.T., and supervised by S.W. R.S., L.M.S., X.G., and R.J.C. grew and characterized bulk WTe_2 crystals. K.W. and T.T. provided hBN crystals. S.W., G.Y., and P.W. wrote the paper with input from all authors.

Competing interests

The authors declare that they have no competing interests.

Data availability

All data needed to evaluate the conclusions in the paper are presented in the paper. Additional data related to this paper are available from the corresponding author upon reasonable request.

Figures

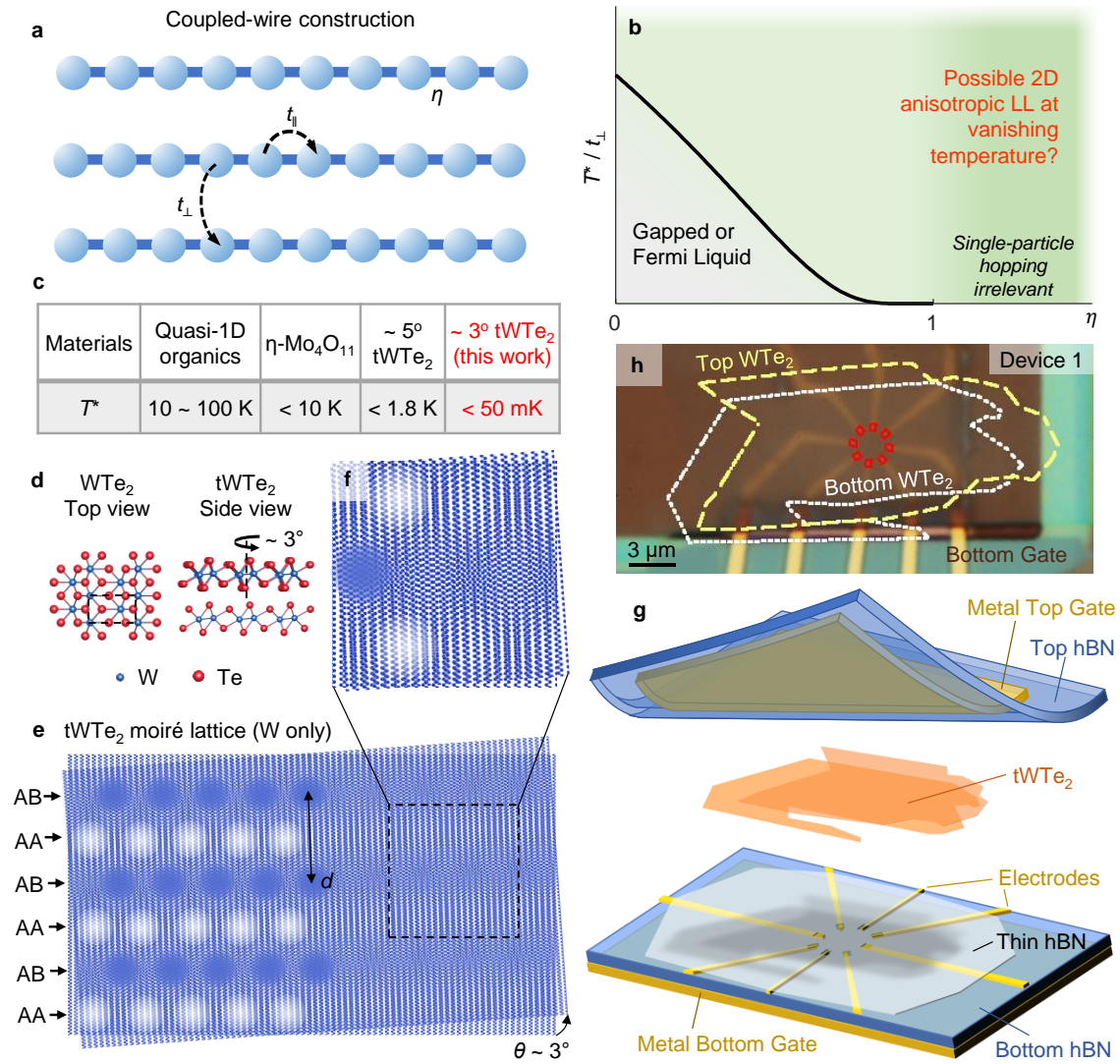


Figure 1 | The coupled-wire construction and tWTe₂ moiré superlattices. **a**, Cartoon illustration of coupled-wire construction, where the interwire (intra-wire) hopping t_{\perp} (t_{\parallel}) and the effective power law exponent η in a single wire is indicated. **b**, A sketch of the 1D-2D crossover temperature T^* *v.s.* η in coupled wires, only considering single particle hopping. **c**, A table of quasi-1D materials that may be related to coupled-wire models. Evidence for LL physics has been reported in these materials at temperatures indicated in the table. Quasi-1D organics, ref. 13, η -MoO₄, ref. 15, $\sim 5^\circ$ tWTe₂, ref. 14. **d**, Left, a top view of monolayer WTe₂, with the unit cell marked by the dashed rectangle. Right, a side view of a tWTe₂ with the top layer rotated by 3° . **e**, Moiré superlattice of tWTe₂ (Only W atoms for a better visualization), showing alternating AB and AA stacking sites. The AA (or AB) sites mimic the coupled-wire construction shown in **a**. **f**, A zoom-in view of the tWTe₂ moiré lattice. **g**, A cartoon illustration of the device structure. See Methods and Extended Data Fig.1 for details about device fabrication. **h**, An optical image of device 1. Yellow dashed line, white dotted line and red solid line indicate respectively the top WTe₂, bottom WTe₂, and the electric contact regions.

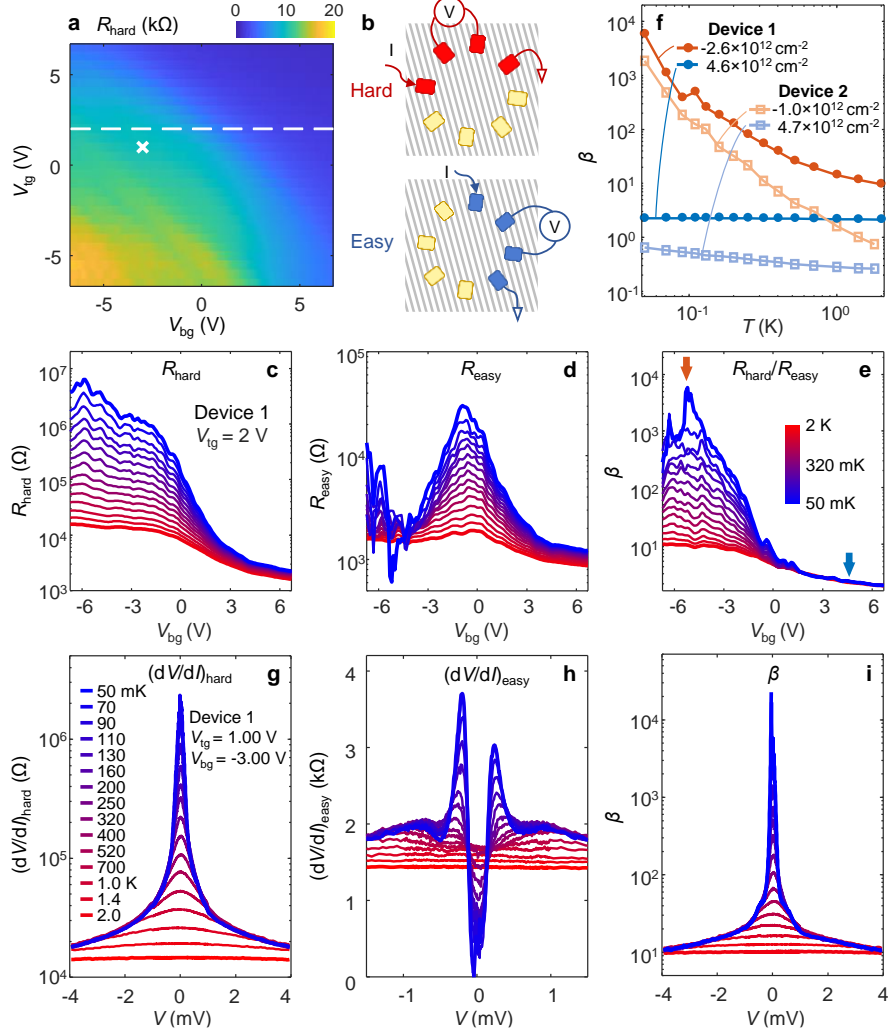


Figure 2 | Exceptional transport anisotropy at millikelvin temperatures. **a**, A dual-gate map of resistance (R_{hard} , geometry shown in **b**) taken in device 1 at 4K. **b**, Cartoon illustration of measurement geometries for R_{hard} and R_{easy} . **c**, R_{hard} *n.s.* V_{bg} taken at various T , ranging from 50 mK (blue) to 2 K (red). See inset in **e** and **g** for temperature legends. V_{tg} is kept at 2 V. **d**, Same measurements as in **c**, but for R_{easy} . **e**, The gate-dependent anisotropy ratio $\beta \equiv R_{\text{hard}}/R_{\text{easy}}$ under various T . Orange (blue) arrow indicates the gate where the orange (blue) curve in **f** is extracted. **f**, β as a function of T , plotted for two typical n_g in electron (hole) side. Data taken in both devices 1 and 2 are shown. **g**, $(dV/dI)_{\text{hard}}$ *n.s.* d.c. bias V at various T . **h**, The same as **g**, but for easy direction. **i**, Bias-dependent anisotropy β at various T .

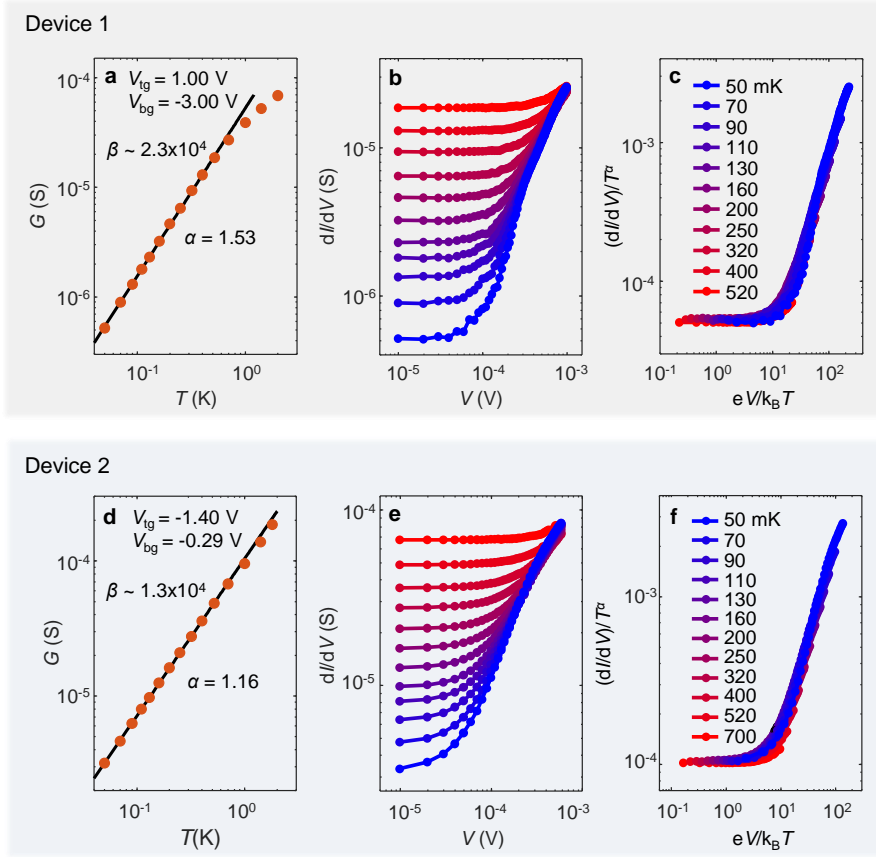


Figure 3 | Luttinger Liquid behaviors down to 50 mK. **a**, G *v.s.* T in a log-log plot taken in device 1 at the same gate configuration as that in Fig. 2g-i. The contact configuration is the same as R_{hard} . The solid line is a power law fit to the low T data, with the resulting exponent α indicated. The corresponding anisotropy β is indicated as well. **b**, dI/dV *v.s.* V at various T , ranging from 50 mK to 520 mK (the same legends as **c**), taken at the same gate voltages as in **a**. **c**, The scaled plot $(dI/dV)/T^\alpha$ *v.s.* $eV/k_B T$ for the same data shown in **b**, using the same α extracted in **a**. **d-f**, the same plots for a selected gate configuration taken in device 2.

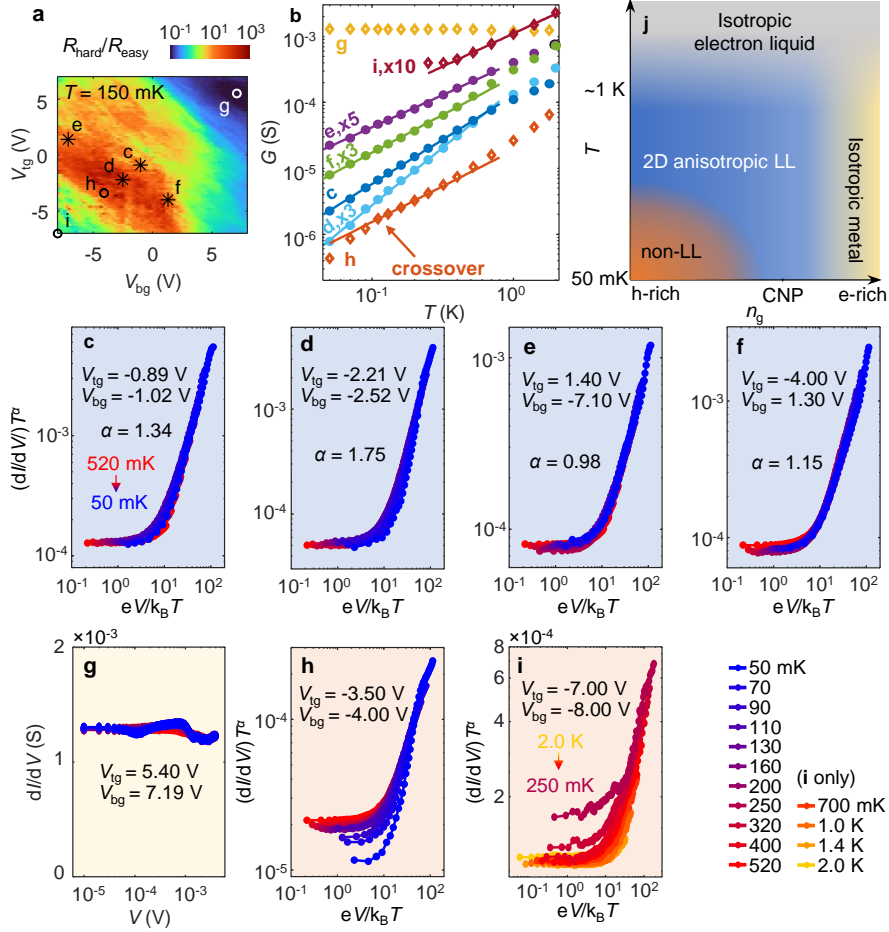
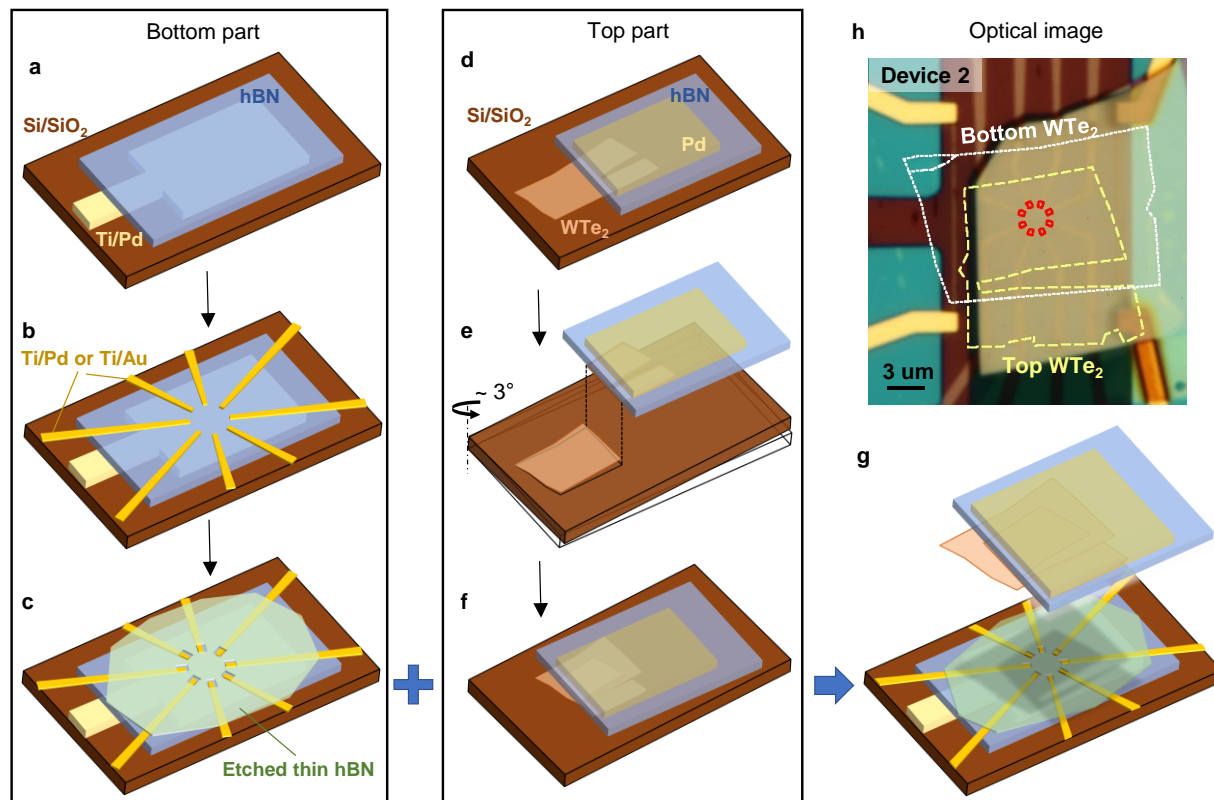
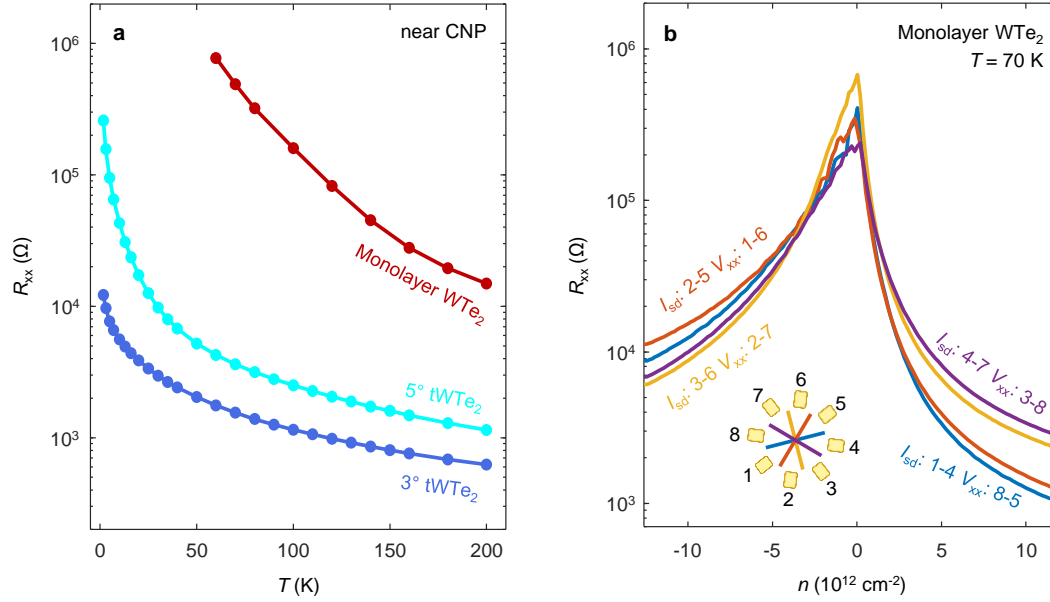


Figure 4 | Electronic phase diagram for the tWTe₂ ($\theta \sim 3^\circ$). **a**, A dual gate map of anisotropy β taken at 150 mK (device 2). **b**, G *v.s.* T at selected gate voltages, corresponding to the spots marked as c-i in **a**. For better visualization, some curves are multiplied by a factor, as indicated next to them. **c-f**, scaled differential conductance plot for the corresponding spots (c-f) in **a**. Excellent power law scaling behaviors are seen, indicating the LL physics. **g**, dI/dV *v.s.* V for spot g (electron-rich region), showing a weak T or V dependence (an Ohmic behavior). **h**, the scaled differential conductance plot for spot h, which develops a clear deviation from the universal scaling. An exponent $\alpha = 1.08$ is used in the plot. **i**, the same scaling plot for spot i, which also develops a deviation from the universal scaling. Data is present down to 250 mK, below which electric contacts become bad at this gate configuration. An exponent $\alpha = 1.00$ is used in the plot. **j**, A preliminary phase diagram for the $\sim 3^\circ$ tWTe₂ system.

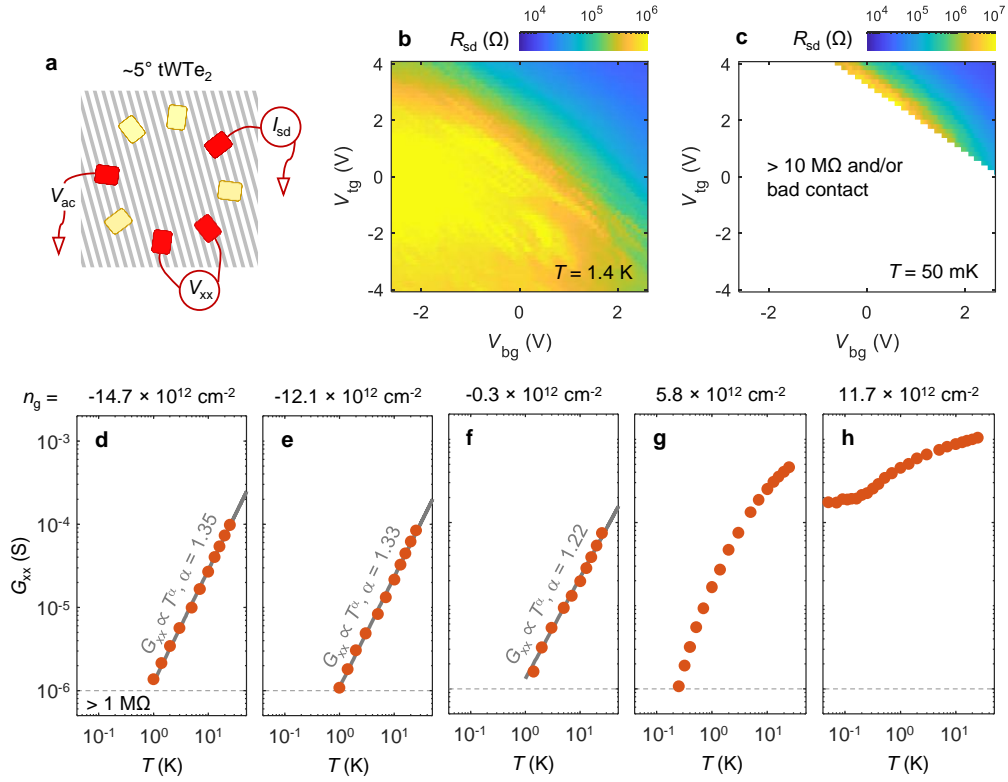
Extended Data Figures



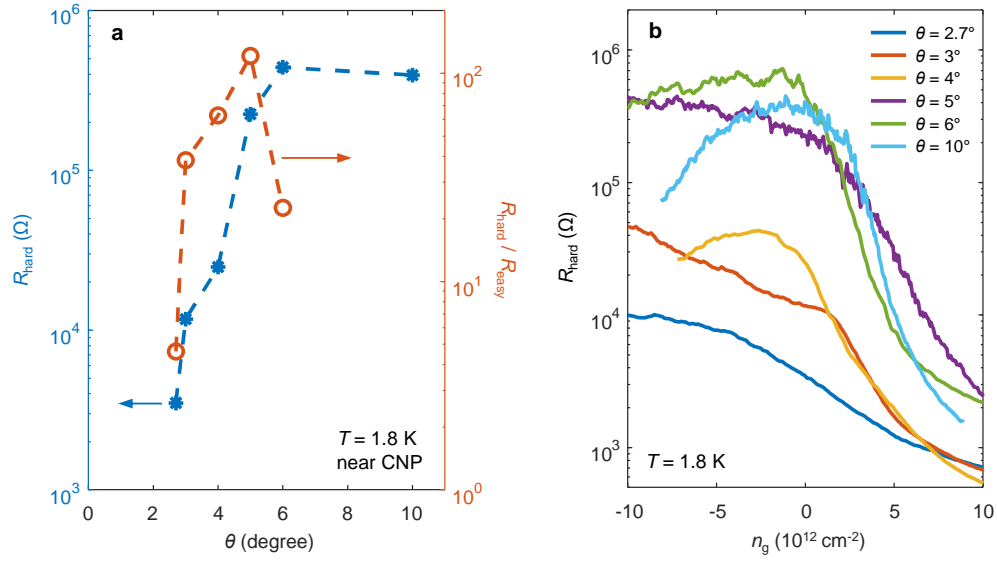
Extended Data Fig. 1 | Cartoon illustration of device fabrication process. **a**, Ti/Pd layer deposited on an insulating Si/SiO₂ substrate, followed by transferring a layer of hBN dielectric for the bottom gate. **b**, Ti/Pd (device 1) or Ti/Au (device 2) electrodes deposited on the bottom hBN. **c**, Thin layer of hBN transferred on electrodes and selectively etched to expose only the ends of electrodes. **d**, Top hBN dielectric and pre-deposited Ti/Pd (device 1, Pd for device 2) layer were picked up and aligned with monolayer WTe₂. **e & f**, Tear-and-stack process for creating the tWTe₂ stack. **g**, Complete the device by stacking the top part onto the prepared bottom part. Steps **d-g** were carried out in an Ar-filled glovebox. **h**, An optical image of device 2. The yellow, white and red lines mark the top WTe₂, bottom WTe₂ and the electric contact regions, respectively.



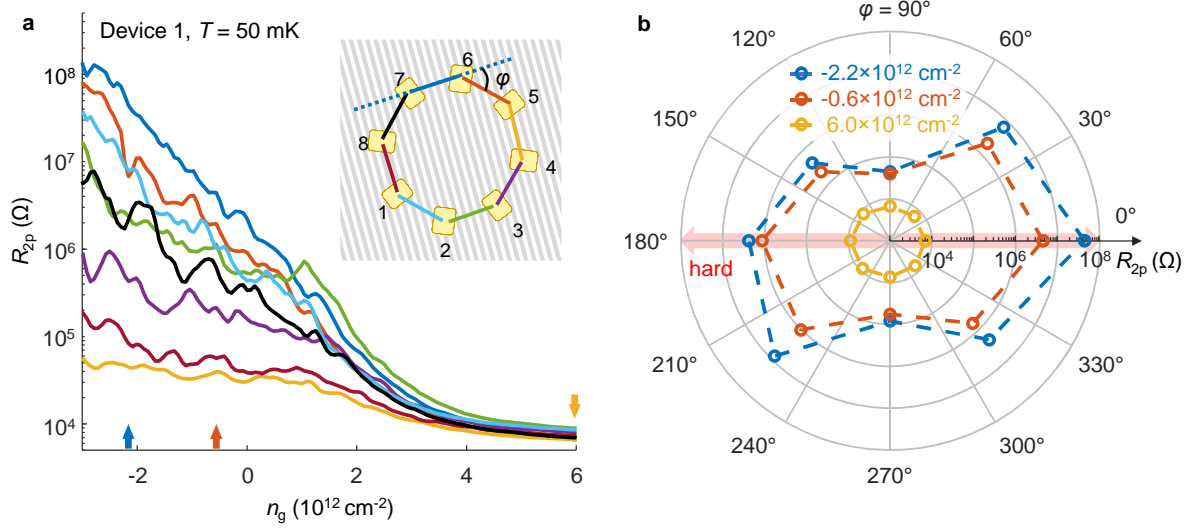
Extended Data Fig. 2 | Comparison between transport behaviors of monolayer WTe_2 , $\sim 3^\circ$ $tWTe_2$ and $\sim 5^\circ$ $tWTe_2$. **a**, Temperature dependent four-probe resistance of the three devices at a doping density near charge neutrality point (CNP). **b**, Typical Four-probe resistances of a monolayer WTe_2 device measured along different in plane directions (contact configurations are shown as inset).



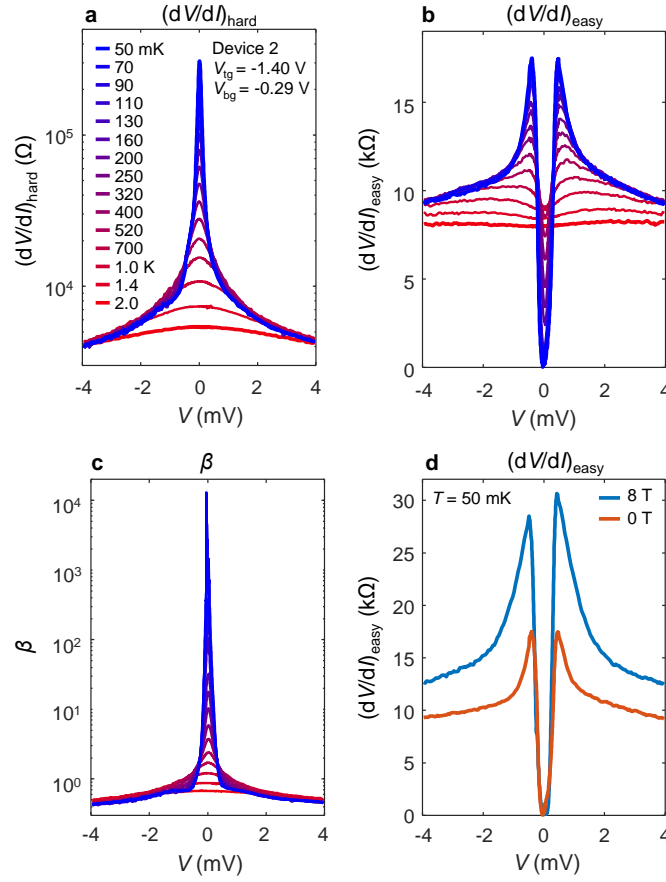
Extended Data Fig. 3 | Behaviors of a 5° tWTe₂ device approaching the millikelvin regime. **a**, An illustration of the measurement configuration. **b**, Two-probe resistance $R_{sd} \equiv V_{ac}/I_{sd}$ as a function of the top and bottom gate voltages at 1.4 K. **c**, The same measurement data but at 50 mK. The white color denotes regions where resistance is too large to be reliably determined or the contact is bad. Note that only a small portion of the gate map on the electron-doping side could be measured reliably down to 50 mK. **d-h**, Temperature dependent four probe resistance $G_{xx} \equiv I_{sd}/V_{xx}$ at selected doping levels. On the hole side, the resistance quickly goes above \sim M Ω , preventing a reliable quantitative analysis of their behaviors at millikelvin.



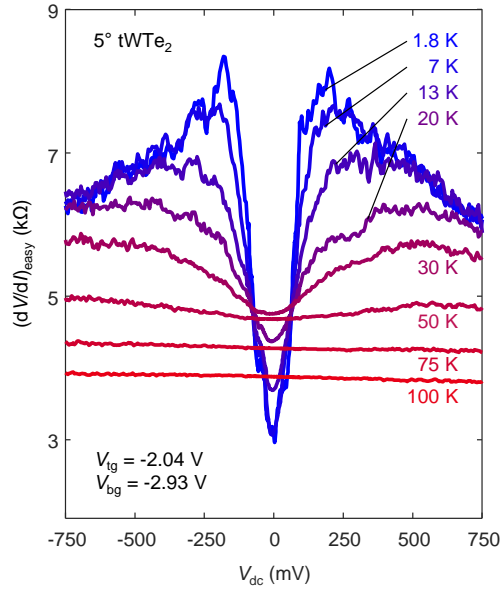
Extended Data Fig. 4 | Effect of twist angle on tWTe₂ devices. **a**, measured four-probe resistance R_{hard} (blue) and extracted anisotropy $R_{\text{hard}}/R_{\text{easy}}$ (orange) at different small twist angles ranging from 2.7° to 10°, measured at 1.8 K near charge neutrality. For each device, the values are determined by measuring the resistance along different in-plane directions and R_{hard} is chosen as the resistance along the relatively hard direction. Note that anisotropy data for the 10° device is missing since it can't be determined due to an imperfection in this specific device. **b**, R_{hard} versus n_g at 1.8 K for each device.



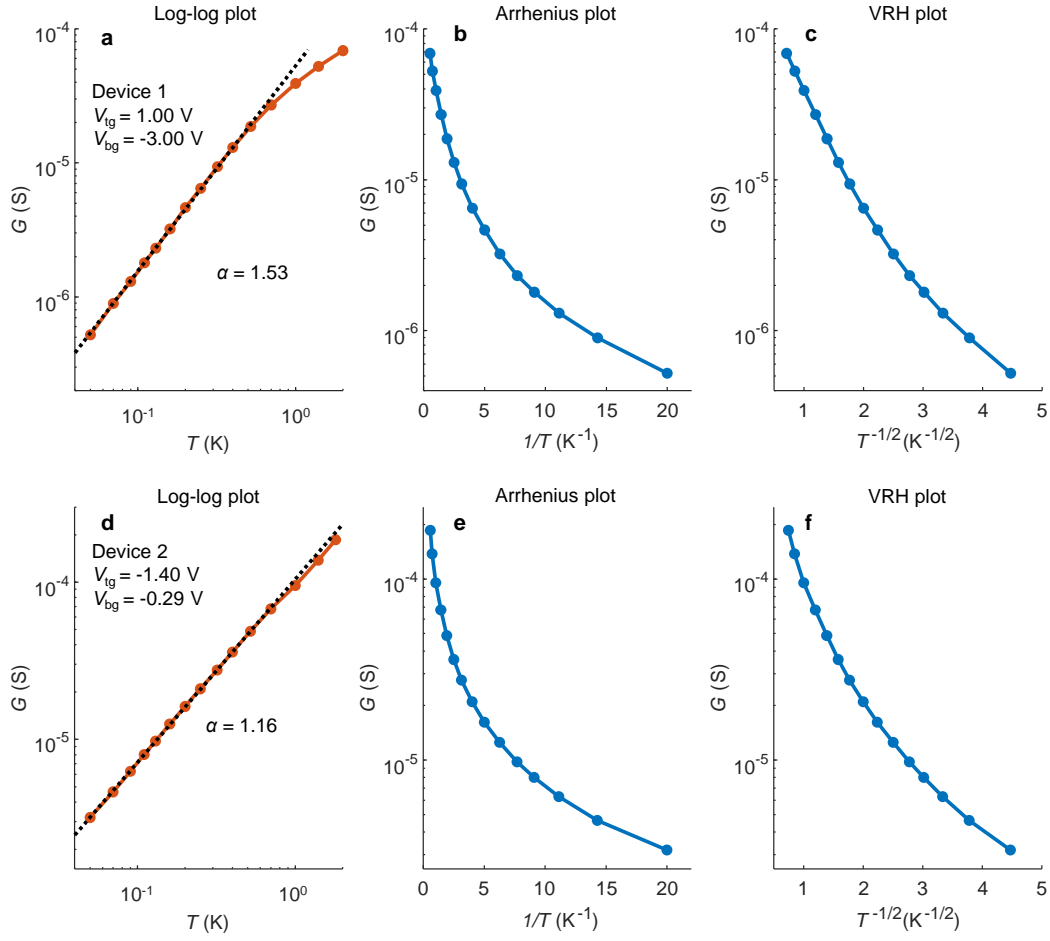
Extended Data Fig. 5 | Transport anisotropy and identifying the hard direction. **a**, Two-probe resistance (R_{2p}) measured between neighboring contacts as a function of n_g . Data were taken in device 1 at 50 mK. Inset illustrates the corresponding pair of probes (connected by a colored solid line) used for each curve, one-to-one matched by their colors. **b**, Identifying the hard direction by the angle dependent two-probe resistance. The direction along the contact pair of 6 and 7 is defined as the reference (0°). Resistance values for all 8 pairs (extracted from **a**) are plotted at three typical n_g , line colors correspond to the arrows in **a**. On the electrode side (yellow), no anisotropy is seen. On the hole side or near charge neutrality (blue and red), exceptionally large anisotropy is seen, and the hard direction can be clearly identified as near 0° (i.e., along contact 6 & 7). The radial axis (R_{2p}) is in log scale.



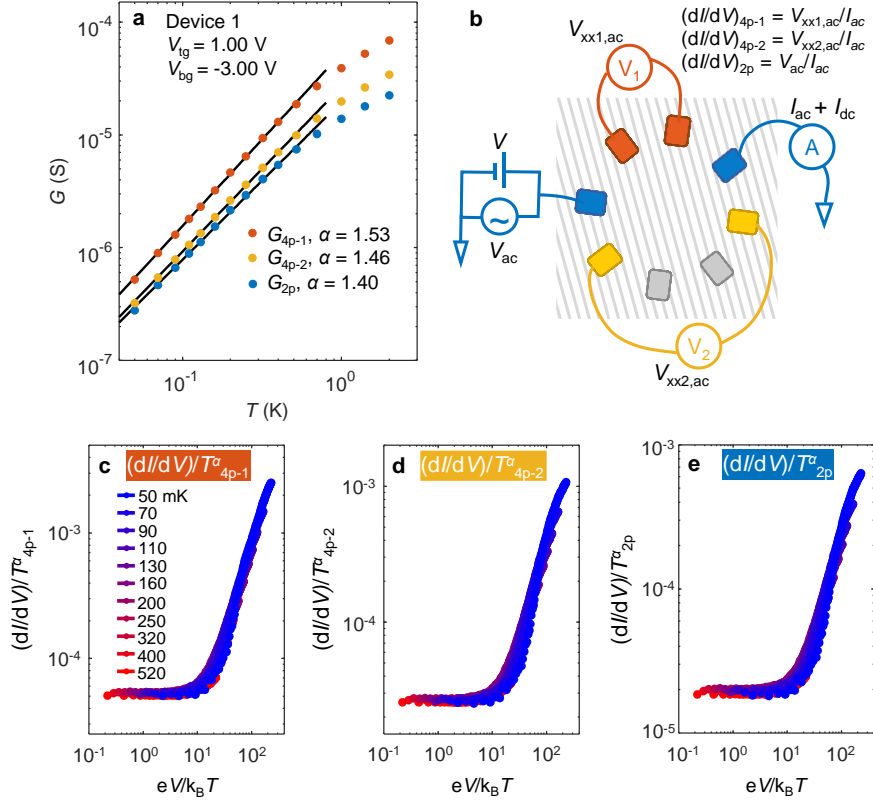
Extended Data Fig. 6 | Transport anisotropy data for device 2. **a**, Differential resistance dV/dI *n.s.* d.c. bias V at various T ranging from 50 mK to 2 K, measured along the hard direction. The gate configuration is chosen as $V_{\text{tg}} = -1.40$ V, $V_{\text{bg}} = -0.29$ V. **b**, The same data but for the measurement taken along the easy direction. **c**, Bias dependent anisotropy at corresponding T . **d**, Magnetic field effect on the differential resistance along the easy direction, at 50 mK.



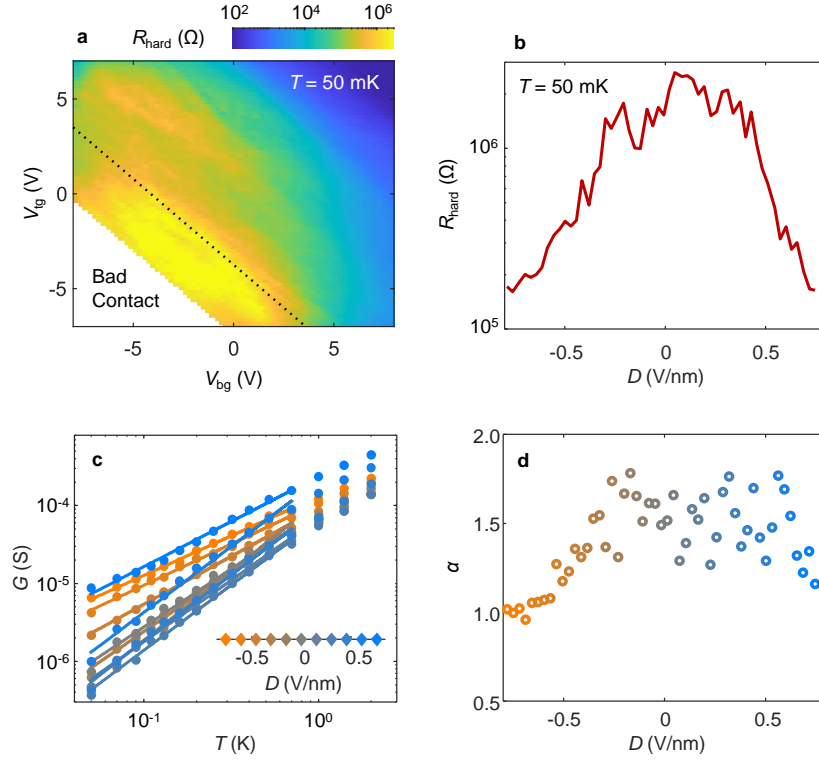
Extended Data Fig. 7 | Differential resistance dV/dI measurement for a 5° tWTe₂ device. dV/dI measured along the easy direction at different temperatures from 1.8 K up to 100 K. A zero-bias dip is developed, similar to the $\sim 3^\circ$ tWTe₂ device reported in the main text. The difference here is that (1) the associated energy scale is larger (as seen by the wider dip in the bias axis) and (2) the zero-bias value doesn't reach zero in this case at 1.8 K.



Extended Data Fig. 8 | Additional plots of conductance data. **a-c**, the same T -dependent conductance data shown in Fig. 3a but displayed in a log-log plot (**a**), an Arrhenius plot (**b**), and a plot against inverse square root of T (**c**). For Luttinger Liquid physics (power-law behavior), it corresponds to $G \propto T^\alpha$; for a band insulator $G \propto \exp(-\Delta/2k_B T)$ and for variable range hopping (VRH) process²⁴ $G \propto \exp(-T^{-1/2})$. Among all three, we find that the power law provides a much better description for data in the low- T regime. **d-f**, the same plots as in **a-c**, but for data shown in Fig. 3d.



Extended Data Fig. 9 | Scaled conductance under different contact geometries. **a**, Conductance G *v.s.* T taken under the same gate configuration as that in Fig. 3 a-c (device 1), but plotting data with three different measurement geometries shown in **b**. The solid lines are the power law fits to the low- T data, all three data sets yield a very similar exponent. **b**, Measurement geometries for data in **a** and **c-e**. Orange data points in **a** correspond to a four-probe geometry (4p-1), with the source and drain contacts labeled in blue while voltage probes labeled in orange. Yellow data points in **a** (4p-2) correspond to the same source-drain contacts but with a different pair of voltage probes (labeled in yellow). Blue data points (2p) correspond to the same source and drain contacts and use the same source-drain contacts as the voltage probes (a two-probe geometry). **c-e**, Scaled conductance plots for the three corresponding measurement geometries. All follow excellent scaling behaviors and an exponent very close to each other.



Extended Data Fig. 10 | Displacement field (D) effect on the LL behavior (Device 2). **a**, Four-probe resistance measured along the hard direction (R_{hard}) at 50 mK. The white color region is where bad contact prevents a reliable measurement at this temperature. **b**, R_{hard} versus D . Data are extracted from **a**, along the dotted line. **c**, Hard-direction conductance G ($\equiv 1/R_{\text{hard}}$) versus T , at different D along the dotted line shown in **a**. D for each colored curve is indicated in the insert. **d**, D -dependent power law component α , extracted from **c**. It appears that the LL behavior is very sensitive to n_g , but not D . At high D ($|D| > 0.5$ V/nm) a drop in α is seen, potentially indicating a transition especially if D is further increased.